A level set-based interface-enriched topology optimization for the design of phononic crystals with smooth boundaries

van den Boom, Sanne J.; Abedi, Reza; van Keulen, Fred; Aragón, Alejandro M.

DOI
10.1016/j.cma.2023.115888

Publication date
2023

Document Version
Final published version

Published in
Computer Methods in Applied Mechanics and Engineering

Citation (APA)
van den Boom, S. J., Abedi, R., van Keulen, F., & Aragón, A. M. (2023). A level set-based interface-enriched topology optimization for the design of phononic crystals with smooth boundaries. *Computer Methods in Applied Mechanics and Engineering*, *408*, Article 115888. https://doi.org/10.1016/j.cma.2023.115888

Available online at www.sciencedirect.com
ScienceDirect
Comput. Methods Appl. Mech. Engrg. 408 (2023) 115888
Computer methods in applied mechanics and engineering
www.elsevier.com/locate/cma

A level set-based interface-enriched topology optimization for the design of phononic crystals with smooth boundaries

Sanne J. van den Boom[a], Reza Abedi[b], Fred van Keulen[a], Alejandro M. Aragón[a,*]

[a] *Faculty of Mechanical, Maritime and Materials Engineering, Delft University of Technology, Mekelweg 2, 2628 CD Delft, The Netherlands*
[b] *Department of Mechanical, Aerospace and Biomedical Engineering, The University of Tennessee at Knoxville/Space Institute, TN, USA*

Received 20 October 2022; received in revised form 3 January 2023; accepted 3 January 2023
Available online 10 March 2023

Abstract

Phononic crystals can be designed to show band gaps—ranges of frequencies whose propagation is strongly attenuated in the material. In essence, their working principle is based on destructive interference of waves reflecting from the periodic arrangement of material interfaces (*i.e.*, Bragg scattering). Consequently, capturing accurately the behavior at material interfaces requires appropriate numerical modeling and computational design techniques. However, the commonly used density-based representation in popular topology optimization methods results in a diffuse staircased boundary. The heavily refined finite element meshes required to compensate for this boundary description results in exceedingly large and expensive optimization problems. In this paper, we demonstrate the adverse effect of the density-based boundary description. Furthermore, we propose a level set-based topology optimization procedure with an enriched finite element method that shows improved performance when compared to the density-based approach.

Keywords: Phononic crystals; Topology optimization; Band gap maximization; Smoothness; Diffuse boundaries

1. Introduction

Since their introduction in the seminal papers by Sigalas and Economou [1,2], and Kushwaha et al. [3], phononic crystals (PnCs) have gained increased attention due to their peculiar effect on traveling waves. Because band gaps can be tuned to any mechanical wavelength, applications can vary from thermal control by operating on the nano scale [4], to seismic engineering on the other side of the wavelength spectrum [5]. These materials can be designed for vibrationless environments [6], and for specialized control over the traveling waves, which can be used for energy harvesting [7,8] and for efficient sound radiation [9]. For instance, these periodic media can be used to develop new sensing technology for the characterization of biological samples and sensitive chemicals [10–12], and are sometimes also combined with photonics to form phoxonic sensors [13]. For an overview of the historical development of phononic crystal research, see the review by Hussein et al. [6], the more recent reviews by Vasileiadis et al. [14] and Muhammad and Lim [15], and the review that focusses on tunable and active PnCs by Wang et al. [16].

* Corresponding author.
E-mail address: A.M.Aragon@tudelft.nl (A.M. Aragón).

https://doi.org/10.1016/j.cma.2023.115888

To design these materials for a specific functionality, *ad hoc* trial-and-error design procedures based on intuition are not an option due to the complexity of the structure in these *band gap materials*. Instead, systematic computational procedures are needed for their design, which can generate candidate solutions and quantitatively discriminate among them. Topology Optimization (TO) [17–20] is a powerful numerical tool widely used for designing complex materials and structures that can be used to unlock the full potential of phononic crystals. A first categorization of TO procedures can be made on whether or not gradient information is used during a numerical optimization process. Single- and multi- objective optimization of phononic crystals has successfully been demonstrated using Non-Gradient-based Topology Optimization (NGTO) techniques, such as Genetic Algorithms (GAs). GAs have been used for maximizing absolute and relative band gaps [21–28], for designing tunable PnCs [29,30], PnCs with prestress [31], PnCs with separate band gaps with different polarizations [32], and PnCs with reduced symmetry [24,33]. GAs have also been used for multiobjective optimization [34], including the optimization for band gaps and thermal expansion [35]. Moreover, they have been used in a two-scale approach [36], and in combination with Kriging [37]. NGTO methods can handle discrete design variables, and can therefore be used to assign a material to each element. Although this avoids diffuse boundaries, these methods generally still suffer from staircasing. Furthermore, NGTO methods are usually population-based, and as such, they require vast computational resources despite being *embarrassingly parallel*. As an alternative to NGTO, machine learning techniques have been introduced in recent years for designing PnCs [38–41].

Gradient-based Topology Optimization (GTO), on the other hand, has the advantage of requiring considerably less function evaluations, although it generally cannot handle discrete design variables. Consequently, simply assigning a discrete material to each element is not possible, and other means of describing the geometry are required. Most commonly, the material properties in each element are continuously interpolated to ensure differentiability. Sigmund and Jensen [42,43] were the first to propose density-based topology optimization for designing both PnC unit cells and finite sized phononic crystals. Density-based TO has been used for maximizing the absolute or relative width of band gaps [44–48], the spatial decay of evanescent waves [49], and the wave attenuation in viscoelastic materials [50]. It has also been used to design PnCs that show self-collimation of elastic waves [51], piezoelectric PnCs [52], PnCs with different properties in different directions [53,54], and PnCs that are robust to imperfections [55–59]. Extensive reviews on the developments of topology optimization of PnCs were written by Yi and Youn [60] and Li et al. [61], where the latter also includes works on the topology optimization of Photonic Crystals (PtCs). Despite its popularity, GTO with a density approach leads to boundary descriptions that are both staircased and diffuse, *i.e.*, they have intermediate (gray) values in the design. These staircased and diffused boundaries can lead to inaccurate modeling during the optimization, and therefore to non-optimal designs. This was recently reported by Dalklint et al. [62], who showed that optimized designs that had large tunable band gaps during density-based optimization showed different bad gaps after postprocessing. After postprocessing they also found band gaps for the strain levels that had full bands during optimization.

Yera et al. [63] combine a level set-based approach with local mesh refinements during the topology optimization to achieve a better mesh resolution near the boundaries. However, this method does not remove the staircasing and intermediate densities, and therefore it does not completely solve the issue of inaccurate boundaries. Alternatively, to avoid staircased boundaries, enriched finite element methods can be used in combination with a level set-based topology optimization approach. The enriched analysis of PnCs was demonstrated by Zhao et al. [64] and van den Boom et al. [65], but to the best of our knowledge, topology optimization of PnCs using an enriched finite element method has not yet been described in literature despite its great potential. Once such procedure is the Interface-enriched Generalized Finite Element Method (IGFEM) [66], which has several advantages over the well known eXtended/Generalized Finite Element Method (X/GFEM) [67–69]. In IGFEM, the approximation used in the standard Finite Element Method (FEM) is enriched with an additional term that accounts for *a priori* knowledge about the kinematics of material interfaces. Contrary to X/GFEM, where enrichment functions are associated to nodes of the standard finite element mesh, IGFEM places enrichments to nodes collocated along discontinuities; this provides considerable benefits over X/GFEM with respect to the enforcement of boundary conditions on non-matching edges and the recovery of smooth reactive tractions in Dirichlet boundaries [65,70–72]. IGFEM has been shown to converge optimally with mesh refinement [66,73], and has previously been demonstrated for the topology optimization for compliance minimization [74], and for the immersed analysis of PnC [65].

In this work we study the importance of smooth and non-diffuse boundaries in the analysis and design of phononic crystals. To that end, we first investigate the influence of a staircased and diffuse boundary description. It

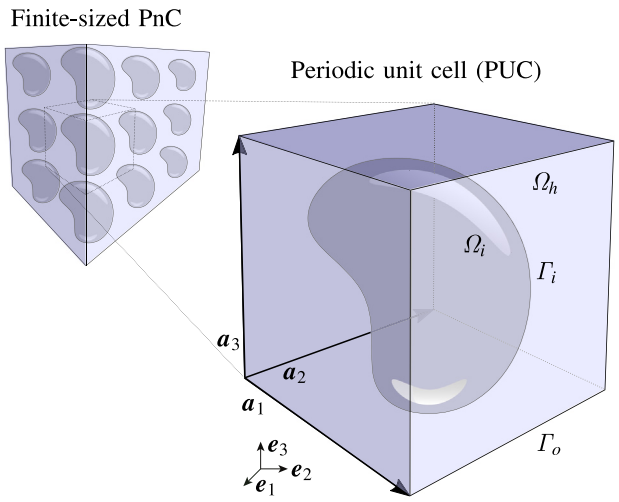

Fig. 1. Schematic representation of a PnC: the finite-sized phononic crystal consists of a periodic array of periodic unit cells. The PUC itself is a cube with lattice vectors $\boldsymbol{a}_1$, $\boldsymbol{a}_2$, and $\boldsymbol{a}_3$. The domain Ω consists of a host phase Ω_h and an inclusion Ω_i. The boundary between the two is denoted Γ_i, and Γ_o is the boundary of the PUC.

is demonstrated that highly refined meshes are needed to reach the same level of accuracy in staircased and diffuse cases. Therefore, a level set-based topology optimization procedure is proposed in combination with IGFEM in order to find optimized unit cell topologies for band gap maximization without staircased boundaries. The topology optimization problem and corresponding sensitivity analysis is discussed in detail. Finally, the procedure is employed to generate optimized phononic crystal topologies with non-staircased boundaries in 2-D and 3-D for band gap maximization. We show that the method can generate designs with band gaps between desired bands, despite numerical challenges.

2. Computational analysis of phononic crystals

The computational analysis of the effect that phononic crystals have on traveling waves can be divided into two categories: approaches considering the full finite-sized phononic crystal, and approaches using a periodic unit cell (PUC), where the PnC is assumed to be infinite. In this paper, the latter approach is used, using the governing equations, modeling approach, and boundary representations described in this section.

Fig. 1 illustrates a 3-D finite-sized PnC and its corresponding PUC. The phononic crystal consists of a periodic array of inclusions Ω_i inside a host material Ω_h, where material interfaces are denoted Γ_i. To obtain this phononic crystal, the PUC is repeated along the lattice vectors $\boldsymbol{a}_1$, $\boldsymbol{a}_2$, and $\boldsymbol{a}_3$.

2.1. Governing equation and formulation

On both the host domain (Ω_h) and the inclusion (Ω_i), the behavior is governed by the elastodynamic wave equation:

$$\rho_j \, \ddot{\boldsymbol{u}}_j - \nabla \boldsymbol{\sigma}_j = \boldsymbol{0} \,, \quad j = h, i, \tag{1}$$

where material density is denoted ρ_j, $\boldsymbol{u}_j(\boldsymbol{x}, t) \equiv \boldsymbol{u}|_{\Omega_j}$ is the restriction of the displacement field $\boldsymbol{u}$ to the domain Ω_j, $\boldsymbol{x}$ indicates spatial coordinate, t indicates time, $\boldsymbol{\sigma}_j = \lambda_j \operatorname{tr}(\boldsymbol{\varepsilon}_j)\boldsymbol{\varepsilon}_j + 2\mu_j \boldsymbol{\varepsilon}_j$ is the stress tensor in the jth phase, $\nabla .$ is the divergence operator, and $\boldsymbol{\varepsilon}_j = \frac{1}{2}\left(\nabla \boldsymbol{u}_j + \nabla \boldsymbol{u}_j^{\mathsf{T}}\right)$ is the linearized strain tensor.

For band structure analysis of PnCs a periodic unit cell is used as illustrated in Fig. 1. Bloch–Floquet periodic boundary conditions are prescribed on the outer boundary Γ_o of this PUC:

$$\boldsymbol{u}(\boldsymbol{x} + \boldsymbol{a}_i, t) = e^{\mathrm{i}(\mathbf{k}\cdot\boldsymbol{a}_i)} \boldsymbol{u}(\boldsymbol{x}, t) \,, \tag{2}$$

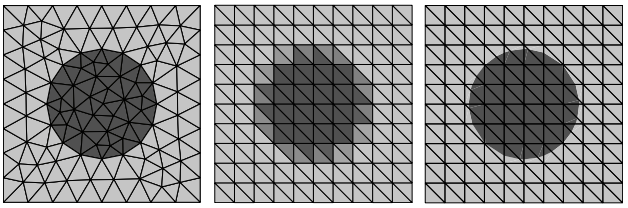

Fig. 2. The three boundary representations used in this paper: the left figure shows a fitted mesh, the middle figure illustrates the density-based approach, and the figure on the right shows an immersed boundary representation.

where $\boldsymbol{a}_i$ is the lattice vector between two periodic edges, i is the imaginary unit, and $\mathbf{k}$ is a wave vector. These boundary conditions enforce periodicity on the displacement field while accommodating for the phase difference of the traveling wave on the two sides of the PUC. The band structure can then be evaluated by performing an eigenvalue analysis for all the wave vectors along the irreducible Brillouin zone [75].

2.2. Boundary representations

Three types of boundary representation are considered in this work, as illustrated in Fig. 2 for a 2-D PUC:

- **Fitted meshes** In these discretizations the material boundary is piece-wise linearly represented by the edges of elements in the mesh. This method would require remeshing in every design iteration in an optimization setting;
- **Density-based meshes** In these meshes, boundaries are represented based on a pseudo-density ρ of the material within each element. A density of 0 is used to represent the host material, while a density of 1 represents the inclusion material. Intermediate density values are assigned to elements that are intersected by the boundary, corresponding to the volume percentage of the element that lies inside the inclusion. For this boundary representation no remeshing is needed during optimization, but the resulting boundaries are staircased and diffuse;
- **Immersed boundaries** The material boundary is decoupled from the analysis mesh by means of IGFEM. This leads to a non-staircased black-and-white piece-wise linear boundary representation. The use of IGFEM for analysis of phononic crystals is described in more detail in the next section and in van den Boom et al. [65].

2.3. Enriched band structure analysis

For the enriched analysis of PnCs, IGFEM is used. Both the trial and test functions in the weak form of (1) are chosen from the same enriched finite element space, where the enriched part of the approximation reproduces the kinematics of a material interface Γ_i, *i.e.*, a discontinuity in the field gradient (a weak discontinuity). The IGFEM approximation is written as

$$\boldsymbol{u}^h(\boldsymbol{x}) = \underbrace{\sum_{i\in\iota_h} N_i(\boldsymbol{x})\,\boldsymbol{U}_i}_{\text{standard FEM}} + \underbrace{\sum_{i\in\iota_w} \psi_i(\boldsymbol{x})\,\boldsymbol{\alpha}_i}_{\text{enrichment}}. \tag{3}$$

The enriched DOFs $\boldsymbol{\alpha}_i$ are associated to new enriched nodes collocated along material interfaces, at the intersection with element edges in the mesh. The material interface is located at the zero contour of a level set function ϕ, that is discretized using the nodes of the background mesh. The location of the intersection $\boldsymbol{x}_l$ between the node locations $\boldsymbol{x}_j$ and $\boldsymbol{x}_k$, with level set values ϕ_j and ϕ_k, respectively, is found as

$$\boldsymbol{x}_l = \boldsymbol{x}_j - \frac{\phi_j}{\phi_k - \phi_j}\left(\boldsymbol{x}_k - \boldsymbol{x}_j\right). \tag{4}$$

Standard FEM procedures can then be employed to obtain the element mass matrix $\boldsymbol{m}_e$ and stiffness matrix $\boldsymbol{k}_e$. For elements that are intersected by a material interface, integration elements are created. In the integration

elements, standard shape functions $\boldsymbol{N}$ of the parent element and enrichment functions $\boldsymbol{\psi}$ are stacked to obtain $\boldsymbol{k}_e$ and $\boldsymbol{m}_e$ as

$$\begin{aligned}\boldsymbol{k}_e &= \int_e j_e \boldsymbol{B}_e^{\mathsf{T}} \boldsymbol{D} \boldsymbol{B}_e \mathrm{d}\xi, \text{ and} \\ \boldsymbol{m}_e &= \int_e j_e \rho_e \begin{bmatrix} \boldsymbol{N} \\ \boldsymbol{\psi} \end{bmatrix} \begin{bmatrix} \boldsymbol{N}^{\mathsf{T}} & \boldsymbol{\psi}^{\mathsf{T}} \end{bmatrix} \mathrm{d}\xi,\end{aligned} \tag{5}$$

where $\boldsymbol{D}$ is the constitutive matrix and ρ_e is the element mass density. The strain-displacement matrix is computed as $\boldsymbol{B}_e = \begin{bmatrix} \boldsymbol{\Delta} N_1 & \boldsymbol{\Delta} N_2 & \dots & \boldsymbol{\Delta} N_n & \boldsymbol{\Delta}\psi_1 & \dots & \boldsymbol{\Delta}\psi_m \end{bmatrix}$, where the differential operator $\boldsymbol{\Delta}$ is defined as:

$$\begin{aligned}\boldsymbol{\Delta} &\equiv \begin{bmatrix} \frac{\partial}{\partial x} & 0 & \frac{\partial}{\partial y} \\ 0 & \frac{\partial}{\partial y} & \frac{\partial}{\partial x} \end{bmatrix}^{\top}, \\ \boldsymbol{\Delta} &\equiv \begin{bmatrix} \frac{\partial}{\partial x} & 0 & 0 & 0 & \frac{\partial}{\partial z} & \frac{\partial}{\partial y} \\ 0 & \frac{\partial}{\partial y} & 0 & \frac{\partial}{\partial z} & 0 & \frac{\partial}{\partial x} \\ 0 & 0 & \frac{\partial}{\partial z} & \frac{\partial}{\partial y} & \frac{\partial}{\partial x} & 0 \end{bmatrix}^{\top},\end{aligned} \tag{6}$$

for 2-D and 3-D, respectively. The derivatives in global coordinates are computed from the derivatives in local coordinates as

$$\nabla_{\mathbf{x}} N_i = \mathbf{J}^{-1} \nabla_{\boldsymbol{\xi}} N_i, \quad \nabla_{\mathbf{x}} \psi_i = \mathbf{J}_e^{-1} \nabla_{\boldsymbol{\xi}} \psi_i, \tag{7}$$

for standard and enriched shape functions, respectively. The determinant and the inverse of the Jacobian of the isoparamatric mapping are denoted j_e and $\boldsymbol{J}_e^{-1}$, and $\boldsymbol{J}^{-1}$ is the inverse of the Jacobian of the mapping of the parent element. The global mass matrix $\boldsymbol{M}$ and stiffness matrix $\boldsymbol{K}$ are subsequently assembled using the standard FEM assembly procedure.

Finally, Bloch–Floquet periodicity, as described in (2), is enforced by a transformation matrix $\boldsymbol{T}$ as

$$\begin{aligned}\tilde{\boldsymbol{K}}(\mathbf{k}) &= \boldsymbol{T}(\mathbf{k})^{\mathsf{H}} \boldsymbol{K} \boldsymbol{T}(\mathbf{k}), \text{ and} \\ \tilde{\boldsymbol{M}}(\mathbf{k}) &= \boldsymbol{T}(\mathbf{k})^{\mathsf{H}} \boldsymbol{M} \boldsymbol{T}(\mathbf{k}),\end{aligned} \tag{8}$$

where $\boldsymbol{T}$ is complex valued and dependent on the wave vector $\mathbf{k}$. A series of eigenvalue analysis is performed to find the band structure, where wave vectors along the edge of the irreducible Brillouin zone are considered:

$$\left(\tilde{\boldsymbol{K}}(\mathbf{k}) - \omega_{\mathbf{k}j}^2 \tilde{\boldsymbol{M}}(\mathbf{k})\right) \tilde{\boldsymbol{V}}_{\mathbf{k}j} = \mathbf{0}. \tag{9}$$

For more details on IGFEM, the reader is referred to Soghrati et al. [66] and Aragón et al. [76]. The IGFEM analysis of immersed phononic crystals is described in more detail in van den Boom et al. [74].

3. Comparison of boundary representations

To illustrate the benefits of piece-wise linear representations in an immersed setting, IGFEM is compared to staircased meshes for a band structure analysis. The effect of these boundary approximations is investigated in Fig. 3 , which shows the predicted band structure for a coarse staircased unit cell (light green) and a unit cell with an immersed representation, analyzed on the same discretization mesh (dark green). Both methods are compared to the results of a very fine standard FEM mesh (black). As apparent from the figure, the band gap obtained by the IGFEM procedure is much closer to the real band gap than the staircased approximation.

Noteworthy, the result given by the enriched formulation requires marginally more DOFs than the result of the density-based approach, because additional enriched nodes are used. However, as these enriched nodes are placed only along the boundary, the number of enriched nodes relative to the number of standard nodes reduces with mesh refinement. To better assess the performance with respect to computational cost, Fig. 4 shows the rate of convergence, where the error in the bands that define the band gap is defined by

$$\epsilon = \sqrt{\frac{1}{|K|N} \frac{\sum_{\mathbf{k}\in K} \sum_j (\omega_{\mathbf{k}j} - \omega^*_{\mathbf{k}j})^2}{\sum_{\mathbf{k}\in K} \sum_j \omega^{*2}_{\mathbf{k}j}}}, \tag{10}$$

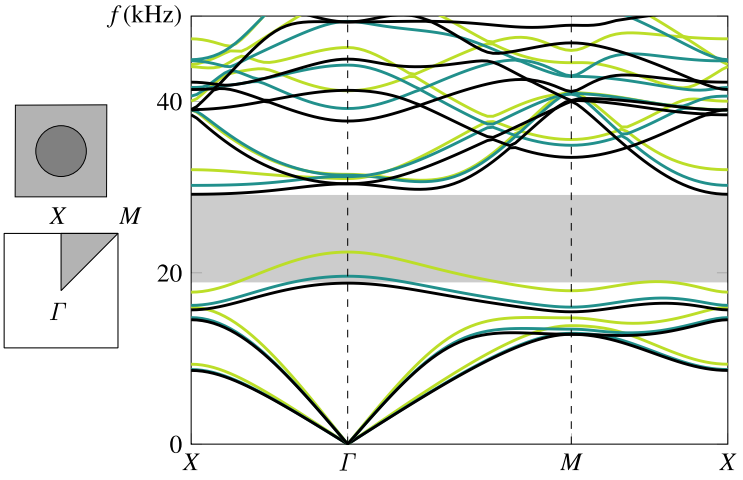

Fig. 3. Comparison of band structures computed with a staircased boundary representation (light green) and a crisp description of the boundary (dark green) to the band structure computed on an overkill matching mesh (black). The band gap for the latter is shown in gray. Clearly, the two approximations show propagation bands within the band gap. For a comparable number of DOFs, the crisp representation performs considerably better than the staircased boundary. On the left, the irreducible Brillouin zone is illustrated. (For interpretation of the references to color in this figure legend, the reader is referred to the web version of this article.)

where K is the set of wave vectors along the irreducible Brillouin zone, with cardinality $|K|$, $\omega^*_{\mathbf{k}j}$ is the jth frequency for wave vector $\mathbf{k}$, obtained by an overkill matching mesh and $\omega_{\mathbf{k}j}$ is the approximated frequency. As apparent from Fig. 4, not only does the IGFEM analysis provide better accuracy, the rate of convergence is also higher. In fact, for some levels of accuracy, the density-based approach requires almost an order of magnitude more DOFs.

The importance of an accurate boundary description for the modeling of phononic crystals is not limited to Bloch–Floquet analysis. This is illustrated in Fig. 5, where the parameter retrieval method [77,78] is used to analyze the dynamic compliance ($D = \mathrm{k}/(Z\omega)$ where Z is the impedance) of the phononic crystal. Here, a coarse staircased representation and a matching mesh with the same element size are compared to a very fine matching mesh. It is clear that the dynamic compliance is not accurately captured with the staircased representation.

To conclude, the use of piece-wise linear representations of the material boundary results in a more accurate solution in the band structure analysis. As a result, much coarser meshes may be used in the analysis and computational design of PnCs. In the context of topology optimization, this does not only drastically reduce the computational effort for the analysis part of the optimization, but it also reduces the number of design variables; this is because in density-based topology optimization, the number of design variables is directly coupled to the number of finite elements. Therefore, level set-based topology optimization using IGFEM may help mitigate to some extent *the curse of dimensionality* in the computational design of phononic crystals.

4. Optimization problem

Now that the importance of using a non-staircased and non-diffuse boundary is demonstrated, a level set-based topology optimization using IGFEM for the boundary description is formulated. In this work we aim to maximize the width of the band gap between the nth and $(n+1)$th propagation bands, on a set of wave vectors K. Henceforward we denote the frequencies corresponding to the nth band that defines the band gap from below $\hat{f}_{\mathbf{k}}$, and the $(n+1)$th, that defines the band gap from above $\check{f}_{\mathbf{k}}$, where $f_{\mathbf{k}} = \omega_{\mathbf{k}}/(2\pi)$. The optimization problem is now formally stated as

$$
\begin{aligned}
\boldsymbol{s}^\star = \arg\min_{\boldsymbol{s}\in\mathcal{D}} \quad & \mathcal{F} = \max\left(\hat{f}_{\mathbf{k}}\right) - \min\left(\check{f}_{\mathbf{k}}\right) \\
\text{such that} \quad & \left(\tilde{\boldsymbol{K}}\left(\mathbf{k},\boldsymbol{s}\right) - \omega^2_{\mathbf{k}j}\tilde{\boldsymbol{M}}\left(\mathbf{k},\boldsymbol{s}\right)\right)\tilde{\boldsymbol{V}}_{\mathbf{k}j} = \mathbf{0} \;\; \forall \mathbf{k} \in K \\
& \boldsymbol{s}_{\min} \leq \boldsymbol{s} \leq \boldsymbol{s}_{\max}.
\end{aligned}
\tag{11}
$$

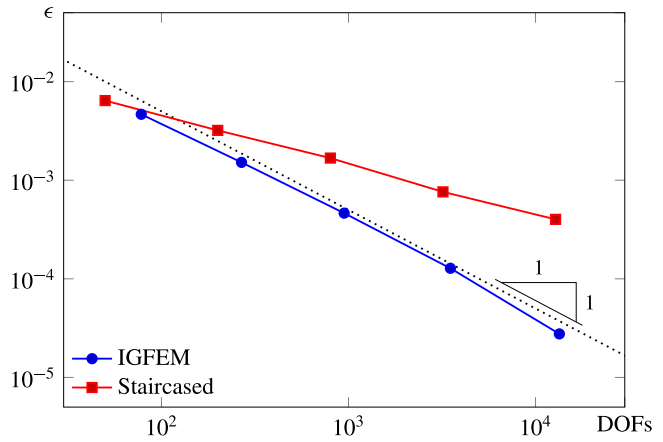

Fig. 4. Convergence of the staircased representation, compared to an enriched formulation using IGFEM. Not only is the enriched representation more accurate, a higher rate of convergence is found.

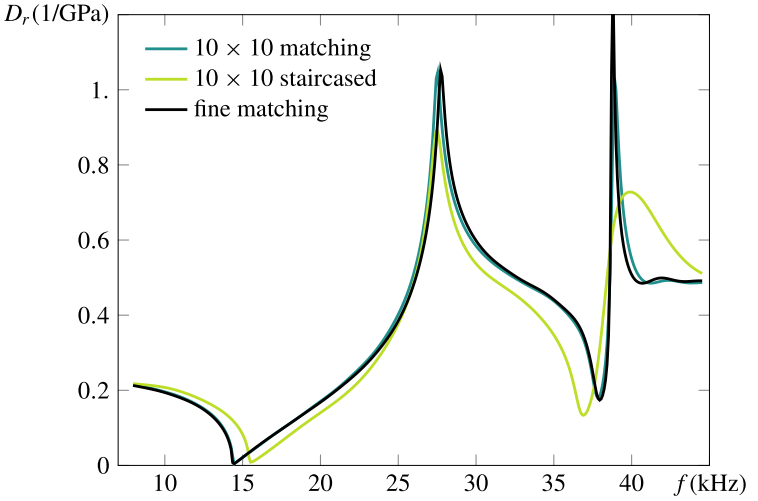

Fig. 5. Retrieved dynamic compliance D_r for staircased representation of a circle and a crisp piece-wise linear representation with the same levels of mesh refinement, compared to the results of a fine matching mesh.

The level set function is parametrized using a number of radial basis functions (RBFs) [74,79], that are scaled using the design variables $\boldsymbol{s}$ (see van den Boom et al. [74]). The value of $\boldsymbol{s}$ is bounded between $\boldsymbol{s}_{\min} = -1$ and $\boldsymbol{s}_{\max} = 1$ to regularize the optimization problem by preventing the level set function from becoming too steep. Note that the optimization problem is self-constrained in the sense that the optimal design does not correspond to a fully empty or a fully filled domain. Therefore, this formulation does not require a volume constraint. It was found that this formulation where the band gap is optimized using $\check{f}_{\mathbf{k}}$ and $\hat{f}_{\mathbf{k}}$ (or $\check{\omega}_{\mathbf{k}}$ and $\hat{\omega}_{\mathbf{k}}$), scales better than using $\check{\omega}^2_{\mathbf{k}}$ and $\hat{\omega}^2_{\mathbf{k}}$ (see Appendix A). A band gap opens up when the objective function is negative.

The maximum operator in Eq. (11) is implemented as the α-smooth max function:

$$S_\alpha\left(\hat{f}_{\mathbf{k}}\right) = \frac{\sum_{\mathbf{k}\in K} \hat{f}_{\mathbf{k}} e^{\alpha \hat{f}_{\mathbf{k}}}}{\sum_{\mathbf{k}\in K} e^{\alpha \hat{f}_{\mathbf{k}}}}, \tag{12}$$

which has the property $S_\alpha\left(\hat{f}_{\mathbf{k}}\right) \to \max$ for $\alpha \to \infty$. Similarly, it tends to a minimum for $\alpha \to -\infty$, and thus, the smooth minimum is implemented analogously. In this work we use $\alpha = 40$ and $\alpha = -40$ for smooth maximum and minimum functions, respectively.

This optimization problem is solved using the Method of Moving Asymptotes (MMA) [80],[1] which is a widely used optimizer in topology optimization. It requires information of the response function values, as well as their gradients or *sensitivities*. The derivation of the sensitivities for band gap maximization can be found in Section 4.1.

4.1. Sensitivity analysis

The objective function described in this paper can be written as a function of the smooth minimum and maximum function as

$$\mathcal{F} = S_\alpha\left(\hat{f}_{\mathbf{k}}\right) - S_{-\alpha}\left(\check{f}_{\mathbf{k}}\right). \tag{13}$$

The derivative of this objective function with respect to the design variables $\boldsymbol{s}$ can be expressed as

$$\frac{\partial \mathcal{F}}{\partial s_i} = \left(\frac{\partial S_\alpha}{\partial \hat{f}_{\mathbf{k}}}\frac{\partial \hat{f}_{\mathbf{k}}}{\partial \hat{\omega}^2_{\mathbf{k}}}\frac{\partial \hat{\omega}^2_{\mathbf{k}}}{\partial \boldsymbol{x}_l} - \frac{\partial S_{-\alpha}}{\partial \check{f}_{\mathbf{k}}}\frac{\partial \check{f}_{\mathbf{k}}}{\partial \check{\omega}^2_{\mathbf{k}}}\frac{\partial \check{\omega}^2_{\mathbf{k}}}{\partial \boldsymbol{x}_l}\right)\frac{\partial \boldsymbol{x}_l}{\partial \phi_j}\frac{\partial \phi_j}{\partial s_i}, \tag{14}$$

where the chain rule is applied. Here, the partial derivative $\partial S_\alpha/\partial f_{\mathbf{k}}$ corresponds to the sensitivity of the smooth maximum/minimum function when an eigenfrequency in the band is changed, $\partial f_{\mathbf{k}}/\partial \omega^2_{\mathbf{k}} = 1/(4\pi\omega)$ describes the sensitivity of the eigenfrequency $f_{\mathbf{k}}$ with respect to the eigenvalue $\omega^2_{\mathbf{k}}$, $\partial \omega^2_{\mathbf{k}}/\partial \boldsymbol{x}_l$ denotes the change in eigenfrequency when an enriched node is moved, $\partial \boldsymbol{x}_l/\partial \phi_j$ are the design velocities, and $\partial \phi_j/\partial s_i$ are the derivatives of the nodal level set values with respect to the design parameters.

First, the derivative of the smooth maximum function can be computed simply as the derivative of Eq. (12):

$$\frac{\partial S_\alpha}{\partial \hat{f}_{\mathbf{k}}} = \frac{e^{\alpha \hat{f}_{\mathbf{k}}}}{\sum_{\mathbf{k}} e^{\alpha \hat{f}_{\mathbf{k}}}}\left(1 + \alpha\left(\hat{f}_{\mathbf{k}} - S_\alpha\right)\right). \tag{15}$$

The derivative of the smooth minimum function is computed analogously.

The derivative of the eigenfrequencies with respect to the enriched node locations $\boldsymbol{x}_l$ can be written as

$$\frac{\partial \omega^2_{\mathbf{k}j}}{\partial \boldsymbol{x}_n} = \frac{1}{m_{jj}}\tilde{\boldsymbol{V}}^{\mathsf{H}}_{\mathbf{k}j}\boldsymbol{T}^{\mathsf{H}}_{\mathbf{k}}\left(\frac{\partial \boldsymbol{K}}{\partial \boldsymbol{x}_l} - \boldsymbol{\omega}^2_{\mathbf{k}j}\frac{\partial \boldsymbol{M}}{\partial \boldsymbol{x}_l}\right)\boldsymbol{T}_{\mathbf{k}}\tilde{\boldsymbol{V}}_{\mathbf{k}j}, \tag{16}$$

where the modal mass $m_{jj} = \tilde{\boldsymbol{V}}^{\mathsf{H}}_{\mathbf{k}i}\boldsymbol{T}^{\mathsf{H}}_{\mathbf{k}}\boldsymbol{M}\boldsymbol{T}_{\mathbf{k}}\tilde{\boldsymbol{V}}_{\mathbf{k}j} = 1$ due to mass orthogonality of the eigenvectors. Note that $\boldsymbol{V}_j = \boldsymbol{T}_{\mathbf{k}}\tilde{\boldsymbol{V}}_{\mathbf{k}j}$, and $\partial \boldsymbol{K}/\partial \boldsymbol{x}_l$ and $\partial \boldsymbol{M}/\partial \boldsymbol{x}_l$ are independent of the wave vector $\mathbf{k}$. Omitting the index j and the dependence on wave vector $\mathbf{k}$ for clarity, this derivative can now be computed element-wise as

$$\frac{\partial \omega^2}{\partial \boldsymbol{x}_l} = \sum_{e\in\iota_l}\boldsymbol{v}^{\mathsf{H}}_e\left(\frac{\partial \boldsymbol{k}_e}{\partial \boldsymbol{x}_l} - \omega^2\frac{\partial \boldsymbol{m}_e}{\partial \boldsymbol{x}_l}\right)\boldsymbol{v}_e, \tag{17}$$

where ι_l denotes the set of integration elements in the support of enriched node $\boldsymbol{x}_l$, and $\boldsymbol{v}_e$ is the part of the eigenvector associated with the element.

The derivative of the element stiffness matrix can be computed as

$$\frac{\partial \boldsymbol{k}_e}{\partial \boldsymbol{x}_n} = \frac{\partial j_e}{\partial \boldsymbol{x}_n}\boldsymbol{B}^{\mathsf{T}}_e\boldsymbol{D}_e\boldsymbol{B}_e + j_e\left(\frac{\partial \boldsymbol{B}^{\mathsf{T}}_e}{\partial \boldsymbol{x}_n}\boldsymbol{D}_e\boldsymbol{B}_e + \boldsymbol{B}^{\mathsf{T}}_e\boldsymbol{D}_e\frac{\partial \boldsymbol{B}_e}{\partial \boldsymbol{x}_n}\right). \tag{18}$$

For the element mass matrix, following a similar approach, the derivative is written as

$$\frac{\partial \boldsymbol{m}_e}{\partial \boldsymbol{x}_n} = \frac{\partial j_e}{\partial \boldsymbol{x}_n}\rho_e\begin{bmatrix}\boldsymbol{N}\\ \boldsymbol{\psi}\end{bmatrix}\begin{bmatrix}\boldsymbol{N}^{\mathsf{T}} & \boldsymbol{\psi}^{\mathsf{T}}\end{bmatrix} + j_e\rho_e\left(\begin{bmatrix}\partial \boldsymbol{N}/\partial \boldsymbol{x}_n\\ \mathbf{0}\end{bmatrix}\begin{bmatrix}\boldsymbol{N}^{\mathsf{T}} & \boldsymbol{\psi}^{\mathsf{T}}\end{bmatrix} + \begin{bmatrix}\boldsymbol{N}\\ \boldsymbol{\psi}\end{bmatrix}\begin{bmatrix}\partial \boldsymbol{N}^{\mathsf{T}}/\partial \boldsymbol{x}_n & \mathbf{0}^{\mathsf{T}}\end{bmatrix}\right). \tag{19}$$

For details on the remaining terms in the sensitivity analysis see Appendix B and van den Boom et al. [74].

5. Optimized phononic crystal designs

The previously described topology optimization procedure is now used to design of phononic crystals in 2-D and 3-D with maximized band gaps.

[1] The author would like to thank Krister Svanberg for providing us with the MMA implementation.

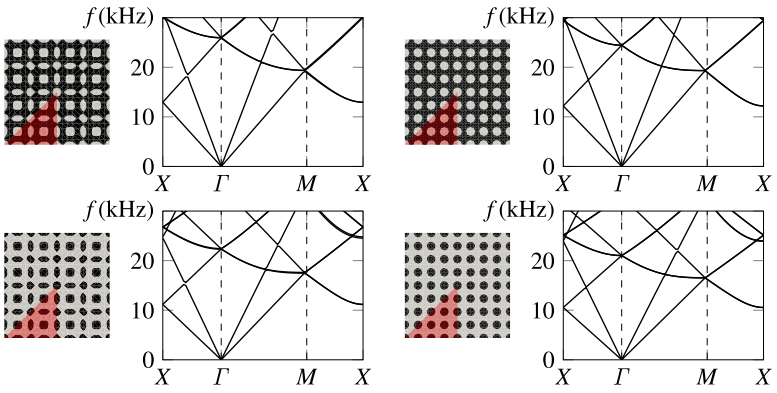

Fig. 6. Initial designs for the 2-D phononic crystal optimization. On the left (right), 20 × 20 × 2 (40 × 40 × 2) triangular elements are used. The top row shows initial conditions with a lead matrix (black) and polycarbonate inclusions(gray). In the bottom row the inclusions (black) are made of lead and the matrix is polycarbonate (gray). The red triangle indicates the reduced design area due to symmetry. (For interpretation of the references to color in this figure legend, the reader is referred to the web version of this article.)

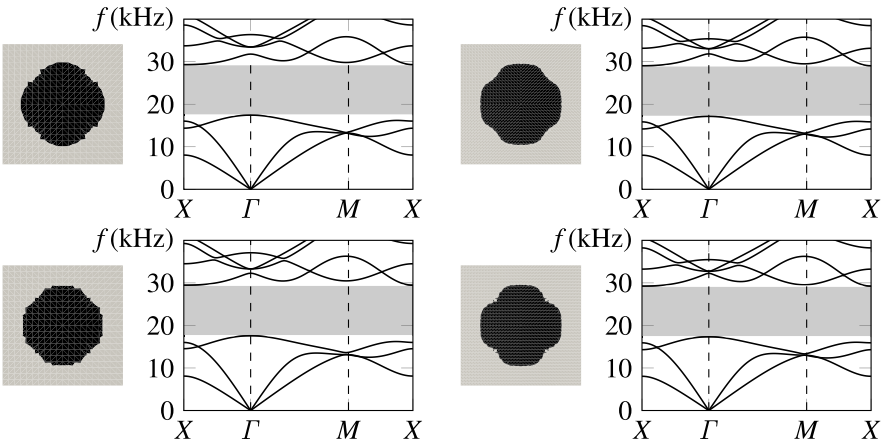

Fig. 7. Optimized results for a band gap maximization between the 3th and 4th bands starting from the initial designs shown in Fig. 6. A large band gap has opened in all four optimizations, and the designs have a similar shape.

5.1. Band gap maximization in 2-D PnCs

First, the maximization of band gaps between different bands in a 2-D PnC is considered. To that end, a square periodic unit cell is optimized with an arbitrary topology that has 8-fold symmetry. The choice of 8-fold symmetry was made to reduce the number of design variables in the optimization problem, to reduce the irreducible Brillouin zone and therefore the numbers of wave vectors that need to be evaluated, and to ensure that the material interfaces will be periodic. The periodic unit cell has dimensions of 25 mm × 25 mm, and consists of polycarbonate ($E_1 = 2.3\,\text{GPa}$, $\nu_1 = 0.37$, $\rho_1 = 1200\,\text{kg/m}^3$) and lead ($E_2 = 16\,\text{GPa}$, $\nu_2 = 0.44$, $\rho_2 = 11\,340\,\text{kg/m}^3$). The phononic crystal is optimized for maximized band gap between the 3th and 4th, and 6th and 7th bands. Because the method cannot nucleate inclusions, initial designs with a number of inclusions are defined. Two types of initial designs are used: lead inclusions in a polycarbonate matrix, and polycarbonate inclusions in a lead matrix. Each optimization problem is solved on two sizes of symmetric triangular meshes, consisting of 20 × 20 × 2 and 40 × 40 × 2 triangular elements, respectively.

The initial designs and their corresponding band structures, without a band gap, are shown in Fig. 6. The red triangles indicate the reduced design area due to the 8-fold symmetry in which the inclusion can be optimized. The full PUC topology is recovered by unfolding the design in this red area. In these figures, the polycarbonate is shown in gray, and lead is shown in black.

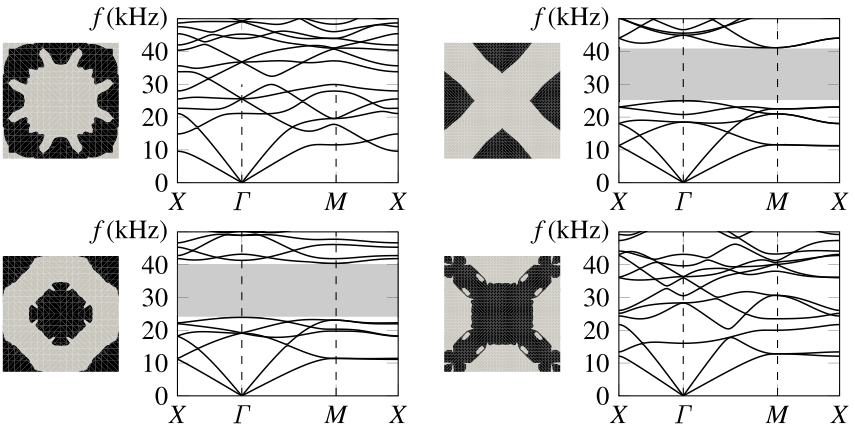

Fig. 8. Optimized results for a band gap maximization between the 6th and 7th bands starting from the initial designs shown in Fig. 6. A large band gap has opened up between these bands for two optimization cases, while in the other two cases no band gap was created.

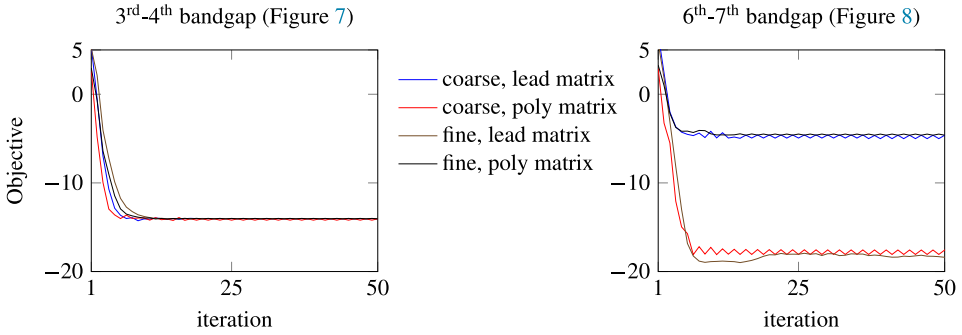

Fig. 9. Convergence of the optimization problems of Figs. 7, and 8. The figure on the left shows the convergence for a band gap between the 3th and 4th bands, the figure on the right show the convergence for a band gap between the 6th and 7th bands.

Figs. 7 and 8 show the optimized designs for maximized band gap between bands 3–4, and 6–7, respectively. For the former, both mesh sizes and both initial designs result in a design that roughly resembles a single circular lead inclusion in a polycarbonate matrix. The band structures show that a large band gap has indeed opened up between the 3th and 4th bands. As demonstrated earlier in Figs. 3 and 4, this design would be poorly represented by a density-based approach. Although all four designs are very similar, they are not exactly the same, indicating that the optimizer has found a local optimum.

The effect of local optima is more clearly observed in the results for band gaps between the 6th and 7th bands. In two of the four cases, the optimizer did not succeed in opening up a band gap. This effect of local optima will be further discussed in Section 6. In the two cases where the optimizer succeeded to create a band gap between the 6th and 7th bands, top right and bottom left, it did so by creating a total of two inclusions in the unit cell. In the case of the top right figure, four halves of the inclusion are visible in the unit cell. The figure on the bottom left has a full inclusion in the center and four quarters in the corners.

Fig. 9 illustrates the convergence of the optimization cases. It is observed that the optimizer converges quickly in all cases, albeit sometimes to a local optimum. Note that the two cases without a band gap still appear to have a negative objective value, which would indicate a band gap. This can be explained by the fact that the smooth minimum and smooth maximum functions that are used in the optimization are approximations of the actual minimum and maximum functions respectively (see (12)). Increasing the value of α in (12) would improve this approximation, but it would simultaneously increase the nonlinearity of the problem, which could lead to instabilities.

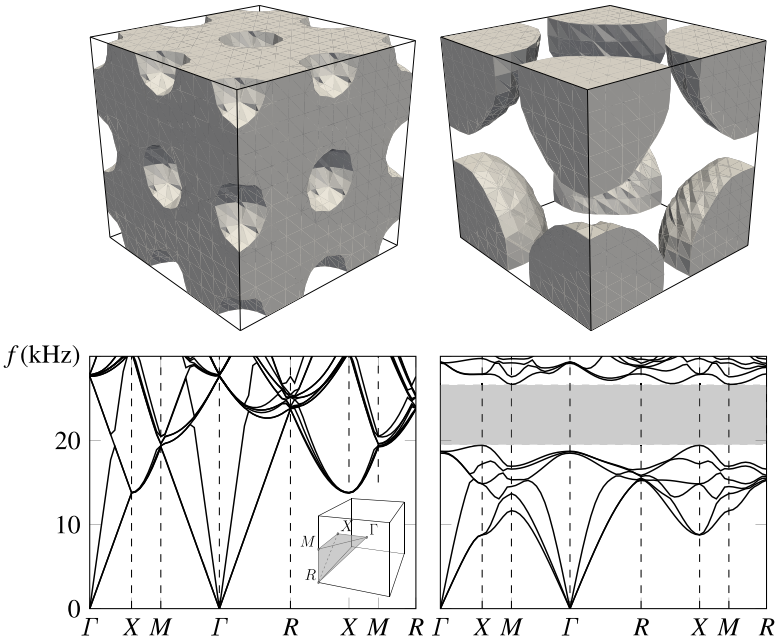

Fig. 10. 3-D results for band gap maximization: On the left the initial design, irreducible Brillouin zone, and corresponding band structure are shown; the right shows the optimized design and band structure with the band gap.

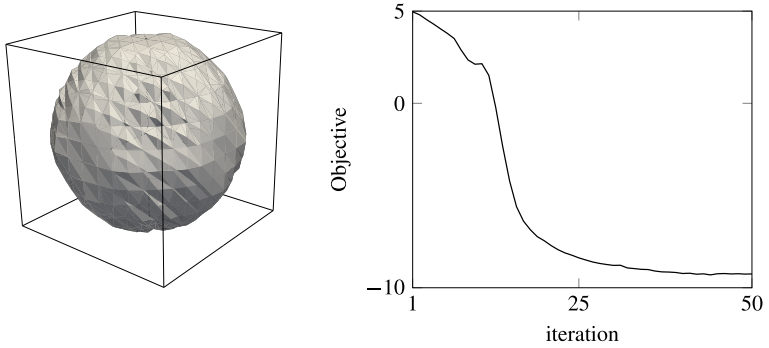

Fig. 11. On the right this figure shows the convergence of the 3D band gap maximization problem, the left shows an alternative representation of the optimized design.

5.2. Band gap maximization in 3-D PnCs

To demonstrate the method for the design of 3-D phononic crystals, a band gap maximization between the 6th and 7th bands is performed for a 3-D periodic unit cell with 48-fold symmetry. This example uses the same material properties and sizes, *i.e.*, a $25 \times 25 \times 25$ mm unit cell, as the previous numerical example. Fig. 10 shows the initial design with polycarbonate inclusions inside a lead matrix, and its corresponding band structure without a band gap. The same figure also shows the final design after 50 iterations and the corresponding band gap. The final design has 8 sections of a single spherical inclusion. In Fig. 11 the convergence of this optimization is shown. Initially, the optimization converges slowly, but after about 15 iterations it rapidly converges to form a large band gap. This figure also shows an alternative representation of the optimized design that more clearly shows that the result resembles a spherical inclusion.

6. Discussion and conclusions

In this work we have shown that the numerical analysis and design of phononic crystals relies heavily on the boundary description of material interfaces. The popular density-based topology optimization method results in staircased and diffuse boundaries that are detrimental for the analysis accuracy in periodic unit cell-based phononic crystals. As shown in this work, highly refined analysis meshes are needed when using a density-based approach to compensate for the loss of accuracy. These highly refined meshes lead to prohibitively expensive optimization problems.

The level set-based topology optimization that uses IGFEM for phononic crystal design proposed in this paper provides an alternative optimization method in which coarser meshes can be used to achieve the same level of accuracy compared to density methods. Furthermore, in this method the design variables are decoupled from the analysis mesh, which further reduces computational costs. The method was demonstrated for full band gap maximization in 2-D and 3-D. However, there are still challenges.

The first observation is the fact that there are many local optima to which the optimizer may converge that may not even show a band gap at all. Small changes in the initial design or the move limit that is used in the MMA may result in a completely different optimized design. To illustrate this, Fig. 12 shows the optimization for a band gap between the 6th and 7th bands. On the left it shows the optimized result that converged to a solution without a band gap. The right shows the same optimization problem, that started from the same initial design, but was optimized using a larger move limit and less wave vectors along the irreducible Brillouin zone. Starting from an initial design with slightly larger inclusions also has a similar effect in that it also results in the desired band gap. This problem may therefore be partially alleviated by using a method to nucleate inclusions in the design, such as using topological derivatives [81].

The initial design and move limit are not the only factors for local optima to occur in the topology optimization of phononic crystals. Fig. 13 shows on the left a 2×2 phononic crystal based on the unit cell that was optimized for a band gap between the 6th and 7th bands. The unit cell with a green outline is the result of a topology optimization as presented in this work. The unit cell that is outlined in blue describes the exact same PnC, and therefore has the exact same performance. The unit cell shown with the red outline cannot be achieved during the optimization due to the symmetry constraints, but it would also have the same performance. In fact, any unit cell of the same dimensions would perform the same. Therefore, the number of local optima is amplified significantly when the symmetry is released. Additionally, reducing the symmetry would lead to another – larger – irreducible Brillouin zone, so more wave vectors should be considered during the optimization, increasing computation time.

Another observation that can be made is that there are small oscillations in the objective function. These oscillations are especially visible in Fig. 9. Several explanations for these oscillations exist. First, as observed in the optimization of lattice-based PnCs in Quinteros et al. [82], the oscillations may be caused by the MMA optimizer, in which case implementing a Globally Convergent Method of Moving Asymptotes (GCMMA) [83] in future work would help. Another possible explanation is found in the fact that the sensitivities are not always accurate during the optimization. As described in van den Boom et al. [74], this can be attributed to the discretization of the level set function. These oscillations can be alleviated by using a smaller move limit, using a finer grid for the level set discretization, or imposing a minimum length scale.

Another reason for inaccurate sensitivities is found in the multiplicity of eigenmodes and mode switching, which occurs often in the highly symmetric unit cells of the PnC. As discussed in Seyranian et al. [84], these multiple eigenvalues are not differentiable in the normal sense but they require instead sensitivity analysis based on a perturbation technique to compute directional derivatives. For simplicity, this was not done in this work, but it could prove beneficial in further developments. Indeed, mode switching is observed in Fig. 12 as illustrated with red circles. Alternatively, Quinteros et al. [82] suggest that mode switching may be avoided when all the lower and upper bands are included in the approximation of the maximum and minimum, respectively.

Despite these challenges, the computational design procedure presented herein enables efficient generation of phononic crystal arrangements for specialized functionalities. Furthermore, the proposed procedure may be extended to other problems that require a smooth description of the boundaries, such as fluid–structure interaction.

Declaration of competing interest

The authors declare that they have no known competing financial interests or personal relationships that could have appeared to influence the work reported in this paper.

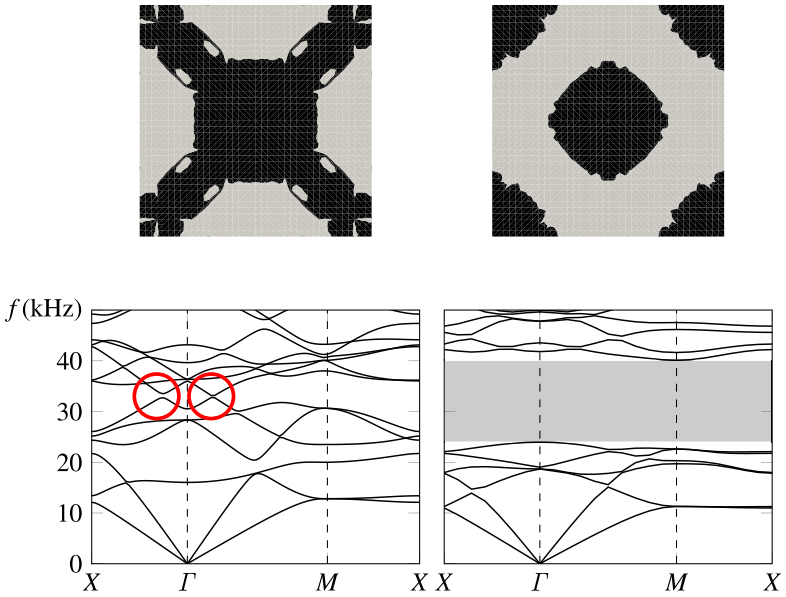

Fig. 12. Band gap optimization for a band gap between the 6th and 7th band. On the left the results are shown for which no band gap opened. The right shows the results for the same optimization problem with a larger move limit and with less wave vectors evaluated along the horizontal axis. The red circles on the left highlight mode switching in the band structure. (For interpretation of the references to color in this figure legend, the reader is referred to the web version of this article.)

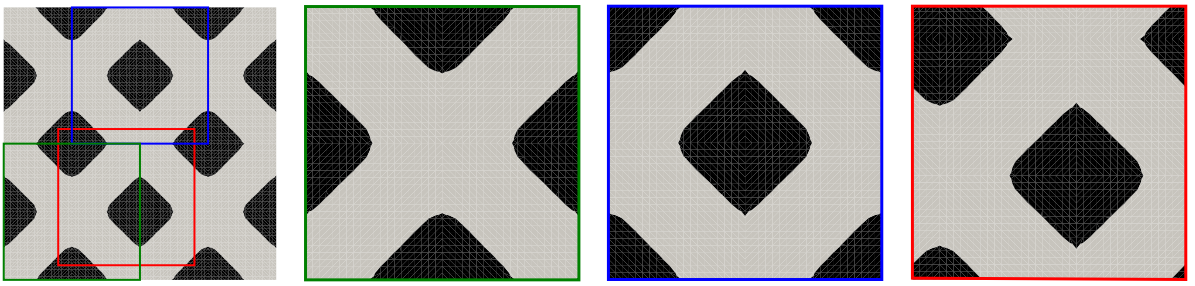

Fig. 13. Illustration of a few periodic unit cells that describe the same PnC, and cause the problem to have many local optima. Due to the symmetry constraint, the unit cell with a red outline cannot be achieved during optimization. (For interpretation of the references to color in this figure legend, the reader is referred to the web version of this article.)

Data availability

No data was used for the research described in the article.

Appendix A. Objective scaling

The objective function for the maximization of absolute and relative bandgaps in literature is sometimes described in terms of ω^2, and sometimes in terms of ω or f. In this appendix it is illustrated why the optimizer converges better when using f (or ω) instead of ω^2. Fig. 14 shows a small 1D PnC that is used for this purpose. It consists of a $L = 25$ mm unit cell with lead and polycarbonate constituents. It is meshed with a single 1D element and the material is described with an IGFEM enrichment at location b. Bloch–Floquet periodic boundary conditions are prescribed to both standard nodes, and the band structure is computed.

Fig. 15 illustrates the scaling of the objective value in terms of ω^2 and f as a function of the location b. In the figure the absolute value of the objective function is shown, and the objective is scaled to 1 for an interface in the

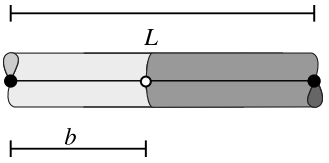

Fig. 14. Small 1D test problem to illustrate the scaling of the objective as a function of the interface location.

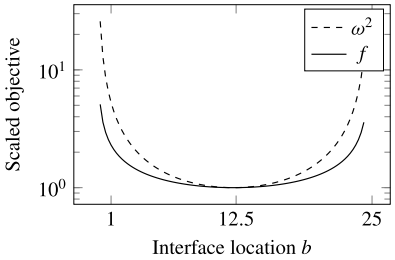

Fig. 15. Scaled objective values as a function of the interface location b.

middle of the unit cell, $b = L/2 = 12.5$ mm. The scaled objective value in terms of ω^2 crosses more than an order of magnitude, while the scaled objective value in terms of f has a less extreme curve. Therefore, in optimization it is preferred to remove the square from the objective function.

Appendix B. Sensitivity analysis

The sensitivity of the $\boldsymbol{B}_e$-matrix with respect to the enriched node location is

$$\frac{\partial \boldsymbol{B}_e}{\partial \boldsymbol{x}_n} = \begin{bmatrix} \boldsymbol{0} & \boldsymbol{0} & \dots & \boldsymbol{0} & \frac{\partial \boldsymbol{\Delta}\psi_1}{\partial \boldsymbol{x}_n} & \dots & \frac{\partial \boldsymbol{\Delta}\psi_m}{\partial \boldsymbol{x}_n} \end{bmatrix}, \tag{20}$$

where the terms can be computed as

$$\frac{\partial \nabla_{\boldsymbol{x}} \psi_i}{\partial \boldsymbol{x}_n} = \frac{\partial \boldsymbol{J}_e^{-1}}{\partial \boldsymbol{x}_n} \nabla_{\boldsymbol{\xi}} \psi_i, \tag{21}$$

and the derivative of the Jacobian determinant can be written as:

$$\frac{\partial j_e}{\partial \boldsymbol{x}_n} = \operatorname{tr}\left(\operatorname{adj}(\boldsymbol{J}_e) \frac{\partial \boldsymbol{J}_e}{\partial \boldsymbol{x}_n} \right), \tag{22}$$

where the adjugate is the transpose of the cofactor matrix of $\boldsymbol{J}_e$. The sensitivity of the Jacobian inverse is computed as

$$\frac{\partial \boldsymbol{J}_e^{-1}}{\partial \boldsymbol{x}_n} = -\boldsymbol{J}_e^{-1} \frac{\partial \boldsymbol{J}_e}{\partial \boldsymbol{x}_n} \boldsymbol{J}_e^{-1}, \tag{23}$$

and the sensitivity of the Jacobian itself is defined as:

$$\frac{\partial \boldsymbol{J}_e}{\partial \boldsymbol{x}_n} = \frac{\partial \boldsymbol{x}_e}{\partial \boldsymbol{x}_n} \frac{\partial \boldsymbol{N}_e}{\partial \boldsymbol{\xi}}, \tag{24}$$

The derivatives of the value of the parent shape function on an integration point with respect to the enriched node location are found as:

$$\frac{\partial \boldsymbol{N}}{\partial \boldsymbol{x}_n} = \frac{\partial \boldsymbol{N}}{\partial \boldsymbol{\xi}_p} \boldsymbol{A}^{-1} \frac{\partial \boldsymbol{x}_e}{\partial \boldsymbol{x}_n} \boldsymbol{N}_e, \tag{25}$$

where $\boldsymbol{A}$ is the isoparametric mapping matrix.

Finally, the design velocities can straightforwardly be found as

$$\frac{\partial \boldsymbol{x}_n}{\partial \phi_j} = -\frac{\phi_k}{\left(\phi_j - \phi_k\right)^2} \left(\boldsymbol{x}_j - \boldsymbol{x}_k \right), \tag{26}$$

and the derivative of the nodal level set values with respect to the design variables $\boldsymbol{s}$ are computed as

$$\frac{\partial \boldsymbol{\phi}}{\partial \boldsymbol{s}} = \boldsymbol{\theta}^{\mathsf{T}}. \tag{27}$$

For more information about the use of RBFs in the level set based topology optimization using IGFEM, see van den Boom et al. [74].

References

[1] M. Sigalas, E.N. Economou, Elastic and acoustic wave band structure, J. Sound Vib. 158 (1992) 377–382.
[2] M. Sigalas, E.N. Economou, Band structure of elastic waves in two dimensional systems, Solid State Commun. 86 (3) (1993) 141–143.
[3] M.S. Kushwaha, P. Halevi, L. Dobrzynski, B. Djafari-Rouhani, Acoustic band structure of periodic elastic composites, Phys. Rev. Lett. 71 (1993) 2022–2025.
[4] B.L. Davis, M.I. Hussein, Nanophononic metamaterial: Thermal conductivity reduction by local resonance, Phys. Rev. Lett. 112 (5) (2014) 055505.
[5] Y. Yan, Z. Cheng, F. Menq, Y.L. Mo, Y. Tang, Z. Shi, Three dimensional periodic foundations for base seismic isolation, Smart Mater. Struct. 24 (7) (2015) 075006.
[6] M.I. Hussein, M.J. Leamy, M. Ruzzene, Dynamics of phononic materials and structures: Historical origins, recent progress, and future outlook, Appl. Mech. Rev. 66 (2014) 040802.
[7] S. Tol, F.L. Degertekin, A. Erturk, 3D-printed phononic crystal lens for elastic wave focusing and energy harvesting, Addit. Manuf. 29 (2019) 100780.
[8] C.-S. Park, Y.C. Shin, S.-H. Jo, H. Yoon, W. Choi, B.D. Youn, M. Kim, Two-dimensional octagonal phononic crystals for highly dense piezoelectric energy harvesting, Nano Energy 57 (2019) 327–337.
[9] J. Jung, C.-H. Jeong, J.S. Jensen, Efficient sound radiation using a bandgap structure, Appl. Phys. Lett. 115 (2019) 041903.
[10] R. Lucklum, J. Li, Phononic crystals for liquid sensor applications, Meas. Sci. Technol. 20 (12) (2009) 124014.
[11] A. Oseev, M. Zubtsov, R. Lucklum, Gasoline properties determination with phononic crystal cavity sensor, Sensors Actuators B 189 (2013) 208–212.
[12] R. Lucklum, N. Mukhin, B.D. Rouhani, Y. Pennec, Phononic crystal sensors: A new class of resonant sensors—Chances and challenges for the determination of liquid properties, Front. Mech. Eng. 7 (2021).
[13] Y. Pennec, Y. Jin, B. Djafari-Rouhani, Phononic and photonic crystals for sensing applications, 52, 2019, pp. 105–145.
[14] T. Vasileiadis, J. Varghese, V. Babacic, J. Gomis-Bresco, D.N. Urrios, B. Graczykowski, Progress and perspectives on phononic crystals, J. Appl. Phys. 129 (2021) 160901.
[15] Muhammad, C.W. Lim, From photonic crystals to seismic metamaterials: A review via phononic crystals and acoustic metamaterials, Arch. Comput. Methods Eng. 29 (2021) 1137–1198.
[16] Y.-F. Wang, Y.-Z. Wang, B. Wu, W. Chen, Y.-S. Wang, Tunable and active phononic crystals and metamaterials, Appl. Mech. Rev. 72 (2020) 040801.
[17] M.P. Bendsøe, N. Kikuchi, Generating optimal topologies in structural design using a homogenization method, Comput. Methods Appl. Mech. Engrg. 71 (2) (1988) 197–224.
[18] O. Sigmund, Design of Material Structures Using Topology Optimization (Ph.D. thesis), Department of Solid Mechanics, Technical University of Denmark, 1994.
[19] H.A. Eschenauer, N. Olhoff, Topology optimization of continuum structures: A review, Appl. Mech. Rev. 54 (4) (2001) 331–390.
[20] G.I.N. Rozvany, A critical review of established methods of structural topology optimization, Struct. Multidiscip. Optim. 37 (2009) 217–237.
[21] G.A. Gazonas, D.S. Weile, R. Wildman, A. Mohan, Genetic algorithm optimization of phononic bandgap structures, Int. J. Solids Struct. 43 (18–19) (2006) 5851–5866.
[22] M.I. Hussein, K. Hamza, G.M. Hulbert, K. Saitou, Optimal synthesis of 2D phononic crystals for broadband frequency isolation, Waves Random Complex Media 17 (4) (2007) 491–510.
[23] O.R. Bilal, M.I. Hussein, Ultrawide phononic band gap for combined in-plane and out-of-plane waves, Phys. Rev. E 84 (6) (2011) 065701.
[24] H.-W. Dong, X.-X. Su, Y.-S. Wang, C. Zhang, Topology optimization of two-dimensional asymmetrical phononic crystals, Phys. Lett. A 378 (4) (2014) 434–441.
[25] S. Hedayatrasa, K. Abhary, M. Uddin, C.-T. Ng, Optimum design of phononic crystal perforated plate structures for widest bandgap of fundamental guided wave modes and maximized in-plane stiffness, J. Mech. Phys. Solids 89 (2016) 31–58.
[26] S. Hedayatrasa, M. Kersemans, K. Abhary, M. Uddin, J.K. Guest, W.V. Paepegem, Maximizing bandgap width and in-plane stiffness of porous phononic plates for tailoring flexural guided waves: Topology optimization and experimental validation, Mech. Mater. 105 (2017) 188–203.
[27] O.R. Bilal, M.I. Hussein, Topology optimization of lattice materials, in: Dynamics of Lattice Materials, John Wiley & Sons, Ltd, 2017, pp. 217–231.
[28] Q. Cheng, H. Guo, Y. Tao, P. Sun, G. Fengxiang, Y. Wang, Topological design of square lattice structure for broad and multiple band gaps in low-frequency range, Extreme Mech. Lett. 35 (2020) 100632.
[29] S. Hedayatrasa, K. Abhary, M.S. Uddin, J.K. Guest, Optimal design of tunable phononic bandgap plates under equibiaxial stretch, Smart Mater. Struct. 25 (2016) 055025.

[30] E. Bortot, O. Amir, G. Shmuel, Topology optimization of dielectric elastomers for wide tunable band gaps, Int. J. Solids Struct. 143 (2018) 262–273.
[31] R.D. Pascalis, T. Donateo, A. Ficarella, W.J. Parnell, Optimal design of phononic media through genetic algorithm-informed pre-stress for the control of antiplane wave propagation, Extreme Mech. Lett. 40 (2020) 100896.
[32] Z.-F. Liu, B. Wu, C. He, Systematic topology optimization of solid-solid phononic crystals for multiple separate band-gaps with different polarizations, Ultrasonics 65 (2016) 249–257.
[33] H.-W. Dong, H.-W. Dong, Y.-S. Wang, Y.-F. Wang, C. Zhang, Reducing symmetry in topology optimization of two-dimensional porous phononic crystals, AIP Adv. 5 (2015) 117149.
[34] W. Xu, J. Ning, Z. Lin, W. Qi, H. Liu, W. Wang, Multi-objective topology optimization of two-dimensional multi-phase microstructure phononic crystals, Mater. Today Commun. 22 (2020) 100801.
[35] X. Zhang, H. Ye, N. Wei, R. Tao, Z. Luo, Design optimization of multifunctional metamaterials with tunable thermal expansion and phononic bandgap, Mater. Des. 209 (2021) 109990.
[36] X. Liang, J. Du, Design of phononic-like structures and band gap tuning by concurrent two-scale topology optimization, Struct. Multidiscip. Optim. 61 (2020) 943–962.
[37] X. Zhang, J. Xing, P. Liu, Y. Luo, Z. Kang, Realization of full and directional band gap design by non-gradient topology optimization in acoustic metamaterials, Extreme Mech. Lett. 42 (2021) 101126.
[38] M. Li, Z. Cheng, G. Jia, Z. Shi, Dimension reduction and surrogate based topology optimization of periodic structures, Compos. Struct. 229 (2019) 111385.
[39] C.-X. Liu, G.-L. Yu, G.-Y. Zhao, Neural networks for inverse design of phononic crystals, AIP Adv. 9 (2019) 085223.
[40] S.M. Sadat, R.Y. Wang, A machine learning based approach for phononic crystal property discovery, J. Appl. Phys. 128 (2020) 025106.
[41] X. Li, S. Ning, Z. Liu, Z. Yan, C. Luo, Z. Zhuang, Designing phononic crystal with anticipated band gap through a deep learning based data-driven method, Comput. Methods Appl. Mech. Engrg. 361 (2020) 112737.
[42] O. Sigmund, J.S. Jensen, Topology optimization of phononic bandgap materials and structures, in: Fifth World Congress on Computational Mechanics, 2002.
[43] O. Sigmund, J.S. Jensen, Systematic design of phononic band-gap materials and structures by topology optimization, Phil. Trans. R. Soc. A 361 (2003) 1001–1019.
[44] C.J. Rupp, A. Evgrafov, K. Maute, M.L. Dunn, Design of phononic materials/structures for surface wave devices using topology optimization, Struct. Multidiscip. Optim. 34 (2007) 111–121.
[45] Y. Lu, Y. Yang, J.K. Guest, A. Srivastava, 3-D phononic crystals with ultra-wide band gaps, Sci. Rep. 7 (2017) 43407.
[46] Y.F. Li, F. Meng, S. Li, B. Jia, S. Zhou, X. Huang, Designing broad phononic band gaps for in-plane modes, Phys. Lett. A 382 (2018) 679–684.
[47] W. Li, F. Meng, Y.F. Li, X. Huang, Topological design of 3D phononic crystals for ultra-wide omnidirectional bandgaps, Struct. Multidiscip. Optim. 60 (2019) 2405–2415.
[48] O. Yuksel, C. Yilmaz, Realization of an ultrawide stop band in a 2-D elastic metamaterial with topologically optimized inertial amplification mechanisms, Int. J. Solids Struct. 203 (2020) 138–150.
[49] Y. Chen, X. Huang, G. Sun, X. Yan, G. Li, Maximizing spatial decay of evanescent waves in phononic crystals by topology optimization, Comput. Struct. 182 (2017) 430–447.
[50] Y. Chen, D. Guo, Y.F. Li, G. Li, X. Huang, Maximizing wave attenuation in viscoelastic phononic crystals by topology optimization, Ultrasonics 94 (2018) 419–429.
[51] J.H. Park, P.S. Ma, Y.Y. Kim, Design of phononic crystals for self-collimation of elastic waves using topology optimization method, Struct. Multidiscip. Optim. 51 (6) (2015) 1199–1209.
[52] S.L. Vatanabe, G.H. Paulino, E.C.N. Silva, Maximizing phononic band gaps in piezocomposite materials by means of topology optimization, J. Acoust. Soc. Am. 136 (2014) 494.
[53] J. He, Z. Kang, Achieving directional propagation of elastic waves via topology optimization, Ultrasonics 82 (2018) 1–10.
[54] Y. Chen, F. Meng, G. Sun, G. Li, X. Huang, X. Huang, Topological design of phononic crystals for unidirectional acoustic transmission, J. Sound Vib. 410 (2017) 103–123.
[55] L. Xie, B. Xia, G. Huang, J. Lei, J. Liu, Topology optimization of phononic crystals with uncertainties, Struct. Multidiscip. Optim. 56 (2017) 1319–1339.
[56] X. Zhang, J. He, A. Takezawa, Z. Kang, Robust topology optimization of phononic crystals with random field uncertainty, Internat. J. Numer. Methods Engrg. 115 (2018) 1154–1173.
[57] L. Xie, J. Liu, G. Huang, W. Zhu, B. Xia, A polynomial-based method for topology optimization of phononic crystals with unknown-but-bounded parameters, Internat. J. Numer. Methods Engrg. 114 (2018) 777–800.
[58] M. Ma, L. Wang, Reliability-based topology optimization framework of two-dimensional phononic crystal band-gap structures based on interval series expansion and mapping conversion method, Int. J. Mech. Sci. 196 (2021) 106265.
[59] X. Zhang, A. Takezawa, Z. Kang, A phase-field based robust topology optimization method for phononic crystals design considering uncertain diffuse regions, Comput. Mater. Sci. 160 (2019) 159–172.
[60] G. Yi, B.D. Youn, A comprehensive survey on topology optimization of phononic crystals, Struct. Multidiscip. Optim. 54 (2016) 1315–1344.
[61] W. Li, F. Meng, Y. Chen, Y.f. Li, X. Huang, Topology optimization of photonic and phononic crystals and metamaterials: A review, Adv. Theory Simul. 2 (7) (2019) 1900017.
[62] A. Dalklint, M. Wallin, K. Bertoldi, D. Tortorelli, Tunable phononic bandgap materials designed via topology optimization, J. Mech. Phys. Solids 163 (2022) 104849.

[63] R. Yera, L. Forzani, C.G. Méndez, A.E. Huespe, A topology optimization algorithm based on topological derivative and level-set function for designing phononic crystals, Eng. Comput. 39 (2021) 354–379.
[64] J. Zhao, Y. Li, W.K. Liu, Predicting band structure of 3D mechanical metamaterials with complex geometry via XFEM, Comput. Mech. 55 (2015) 659–672.
[65] S.J. van den Boom, F. van Keulen, A.M. Aragón, Fully decoupling geometry from discretization in the Bloch–Floquet finite element analysis of phononic crystals, Comput. Methods Appl. Mech. Engrg. 382 (2021) 113848.
[66] S. Soghrati, A.M. Aragón, C. Armando Duarte, P.H. Geubelle, An interface-enriched generalized FEM for problems with discontinuous gradient fields, Internat. J. Numer. Methods Engrg. 89 (2012) 991–1008.
[67] T. Belytschko, S.P. Xiao, C. Parimi, Topology optimization with implicit functions and regularization, Internat. J. Numer. Methods Engrg. 57 (8) (2003) 1177–1196.
[68] C.H. Villanueva, K. Maute, Density and level set-XFEM schemes for topology optimization of 3-D structures, Comput. Mech. 54 (2014) 133–150.
[69] P. Liu, Y. Luo, Z. Kang, Multi-material topology optimization considering interface behavior via XFEM and level set method, Comput. Methods Appl. Mech. Engrg. 308 (2016) 113–133.
[70] A. Cuba Ramos, A.M. Aragón, S. Soghrati, P.H. Geubelle, J.-F. Molinari, A new formulation for imposing Dirichlet boundary conditions on non-matching meshes, Internat. J. Numer. Methods Engrg. 103 (6) (2015) 430–444.
[71] A.M. Aragón, A. Simone, The discontinuity-enriched finite element method, Internat. J. Numer. Methods Engrg. 112 (11) (2017) 1589–1613.
[72] S.J. van den Boom, J. Zhang, F. van Keulen, A.M. Aragón, A stable interface-enriched formulation for immersed domains with strong enforcement of essential boundary conditions, Internat. J. Numer. Methods Engrg. 120 (10) (2019) 1163–1183.
[73] S. Soghrati, P.H. Geubelle, A 3D interface-enriched generalized finite element method for weakly discontinuous problems with complex internal geometries, Comput. Methods Appl. Mech. Engrg. 217–220 (2012) 46–57.
[74] S.J. van den Boom, J. Zhang, F. van Keulen, A.M. Aragón, An interface-enriched generalized finite element method for level set-based topology optimization, Struct. Multidiscip. Optim. 63 (2021) 1–20.
[75] L. Brillouin, Les électrons dans les métaux et le classement des ondes de de broglie correspondantes, C. R. Hebd. Seances Acad. Sci. (1930) 191:192.
[76] A.M. Aragón, B. Liang, H. Ahmadian, S. Soghrati, On the stability and interpolating properties of the hierarchical interface-enriched finite element method, Comput. Methods Appl. Mech. Engrg. 362 (2020) 112671.
[77] R. Abedi, A.V. Amirkhizi, Use of loss limit approach to zero in scattering-based parameter retrieval of elastic micro-structured media, Int. J. Solids Struct. 200–201 (2020) 34–63.
[78] A.V. Amirkhizi, Homogenization of layered media based on scattering response and field integration, Mech. Mater. 114 (2017) 76–87.
[79] S. Wang, M.Y. Wang, Radial basis functions and level set method for structural topology optimization, Internat. J. Numer. Methods Engrg. 65 (12) (2006) 2060–2090.
[80] K. Svanberg, The method of moving asymptotes—a new method for structural optimization, Internat. J. Numer. Methods Engrg. 24 (2) (1987) 359–373.
[81] S. Amstutz, H. Andrä, A new algorithm for topology optimization using a level-set method, J. Comput. Phys. 216 (2) (2006) 573–588.
[82] L. Quinteros, V. Meruane, E. Cardoso, Phononic band gap optimization in truss-like cellular structures using smooth P-norm approximations, Struct. Multidiscip. Optim. 64 (2021) 113–124.
[83] K. Svanberg, A class of globally convergent optimization methods based on conservative convex separable approximations, SIAM J. Optim. 12 (2) (2002) 555–573.
[84] A.P. Seyranian, E. Lund, N. Olhoff, Multiple eigenvalues in structural optimization problems, Struct. Optim. 8 (1994) 207–227.